

Article

CO₂-Tolerant Oxygen Permeation Membranes Containing Transition Metals as Sintering Aids with High Oxygen Permeability

Xiaopeng Wang^{1,†}, Lei Shi^{1,†}, Yanhao Huang¹, Lingyong Zeng¹, Mebrouka Boubeche¹ , Dongcheng Li¹ and Huixia Luo^{1,2,3,4,*}

¹ School of Materials Science and Engineering, Sun Yat-Sen University, No. 135, Xingang Xi Road, Guangzhou 510275, China; wangxp27@mail2.sysu.edu.cn (X.W.); shilei8@mail2.sysu.edu.cn (L.S.); huangyh296@mail2.sysu.edu.cn (Y.H.); zengly25@mail2.sysu.edu.cn (L.Z.); boubeche@mail.sysu.edu.cn (M.B.); lidch8@mail2.sysu.edu.cn (D.L.)

² State Key Laboratory of Optoelectronic Materials and Technologies, No. 135, Xingang Xi Road, Guangzhou 510275, China

³ Key Lab of Polymer Composite and Functional Materials, Sun Yat-Sen University, No. 135, Xingang Xi Road, Guangzhou 510275, China

⁴ Guangzhou Key Laboratory of Flexible Electronic Materials and Wearable Devices, Sun Yat-Sen University, No. 135, Xingang Xi Road, Guangzhou 510275, China

* Correspondence: luohx7@mail.sysu.edu.cn; Tel.: +86-020-3938-6124

† These authors contributed equally to this work.



Citation: Wang, X.; Shi, L.; Huang, Y.; Zeng, L.; Boubeche, M.; Li, D.; Luo, H. CO₂-Tolerant Oxygen Permeation Membranes Containing Transition Metals as Sintering Aids with High Oxygen Permeability. *Processes* **2021**, *9*, 528. <https://doi.org/10.3390/pr9030528>

Academic Editor: Nariman Yousefi

Received: 10 February 2021

Accepted: 11 March 2021

Published: 15 March 2021

Publisher's Note: MDPI stays neutral with regard to jurisdictional claims in published maps and institutional affiliations.



Copyright: © 2021 by the authors. Licensee MDPI, Basel, Switzerland. This article is an open access article distributed under the terms and conditions of the Creative Commons Attribution (CC BY) license (<https://creativecommons.org/licenses/by/4.0/>).

Abstract: Chemical doping of ceramic oxides may provide a possible route for realizing high-efficient oxygen transport membranes. Herein, we present a study of the previously unreported dual-phase mixed-conducting oxygen-permeable membranes with the compositions of 60 wt.% Ce_{0.85}Pr_{0.1}M_{0.05}O_{2-δ}-40 wt.%Pr_{0.6}Sr_{0.4}Fe_{0.8}Al_{0.2}O_{3-δ} (M = Fe, Co, Ni, Cu) (CPM-PSFA) adding sintering aids, which is expected to not only improve the electronic conductivity of fluorite phase, but also reduce the sintering temperature and improve the sintering properties of the membranes. X-ray powder diffraction (XRD) results indicate that the CPM-PSFA contain only the fluorite and perovskite two phases, implying that they are successfully prepared with a modified Pechini method. Backscattered scanning electron microscopy (BSEM) results further confirm that two phases are evenly distributed, and the membranes are very dense after sintering at 1275 °C for 5 h, which is much lower than that (1450 °C, 5 h) of the composite 60 wt.%Ce_{0.9}Pr_{0.1}O_{2-δ}-40 wt.%Pr_{0.6}Sr_{0.4}Fe_{0.8}Al_{0.2}O_{3-δ} (CP-PSFA) without sintering aids. The results of oxygen permeability test demonstrate that the oxygen permeation flux through the CPCu-PSFA and CPCo-PSFA is higher than that of undoped CP-PSFA and can maintain stable oxygen permeability for a long time under pure CO₂ operation condition. Our results imply that these composite membranes with high oxygen permeability and stability provide potential candidates for the application in oxygen separation, solid oxide fuel cell (SOFC), and oxy-fuel combustion based on carbon dioxide capture.

Keywords: oxygen separation; composite membrane; al-containing oxides; modified one-pot Pechini method; sintering aids

1. Introduction

There has long been interest in ceramic mixed-conducting oxygen transport membranes (OTMs) technology in virtue of their widespread applications in the energy catalytic fields such as air separation [1–4], cathodes in solid oxide fuel cells (SOFCs) [5,6], hydrocarbons conversion [7–9], hydrogen separation/production [10–13], and oxy-fuel combustion for CO₂ capture [14–18]. Especially, the OTMs with high CO₂ tolerance have great prospects to be used in oxy-fuel combustion integrated with CO₂ capture, which provides an effective way to minimize the emission of CO₂ and toxic NO_x pollutants from

the fossil-fuel power station [17–19]. In this regard, among the mixed-conducting OTMs, recent attention to the development and application of dual-phase membranes has been growing exponentially due to their superior chemical and physical stability compared with the single-phase OTMs. The earliest discovery of dual-phase membranes was using noble metals as the electron-conducting (EC) phases and ceramic perovskite oxides as the pure oxygen ion-conducting (OIC) phases [20]. However, the high cost and mismatch between the conducting coefficients of two phases impeded their industrial application. In order to reduce costs and improve the oxygen permeability, researchers have proposed to use ceramic oxides instead of noble metals being as EC phases. Hence the noble-metal free dual-phase membranes usually consist of ceramic oxide electron conductor (EC) and oxygen ion conductor (OIC) [21–34].

During the exploration of a new dual-phase membrane, researchers have realized that doped CeO_2 oxides are good candidates used as OIC phase in the dual-phase OTMs due to the following aspects: (i) Ce^{4+} in CeO_2 fluorite phase is easy to be reduced to Ce^{3+} under low-oxygen partial pressure or reduction environment, resulting in a large number of oxygen vacancies in the material, showing n -type conductivity and good oxygen ion conductivity in high temperature environment [35]. (ii) CeO_2 has strong tolerance to the dissolution of other oxides, which will introduce more oxygen vacancies inside the material, resulting in a larger electrolysis zone [36]. (iii) CeO_2 based oxides are insusceptible of corrosive gas (H_2S , CO_2 , and SO_2) atmospheres [37,38]. In view of these aforementioned characteristics, CeO_2 has been widely adopted as OIC phase in the dual-phase OTMs. So far, abundant works on the CeO_2 -based dual-phase materials has been reported, such as $\text{Ce}_{0.9}\text{Pr}_{0.1}\text{O}_{2-\delta}$ - $\text{NiFe}_2\text{O}_{4-\delta}$ (CP-NF), $\text{Ce}_{0.8}\text{Tb}_{0.2}\text{O}_{2-\delta}$ - $\text{NiFe}_2\text{O}_{4-\delta}$ (CT-NF), $\text{Ce}_{0.9}\text{Pr}_{0.1}\text{O}_{2-\delta}$ - $\text{Pr}_{0.6}\text{Sr}_{0.4}\text{FeO}_{3-\delta}$ (CP-PSF), $\text{Ce}_{0.85}\text{Sm}_{0.15}\text{O}_{1.925}$ - $\text{Sm}_{0.6}\text{Sr}_{0.4}\text{Al}_{0.3}\text{Fe}_{0.7}\text{O}_{3-\delta}$ (CS-NSAF), $\text{Ce}_{0.8}\text{Gd}_{0.2}\text{O}_{2-\delta}$ - $\text{Ba}_{0.95}\text{La}_{0.05}\text{Fe}_{1-x}\text{Nb}_x\text{O}_{3-\delta}$ (CG-BLFN), and $\text{Ce}_{0.9}\text{Nd}_{0.1}\text{O}_{2-\delta}$ - $\text{Nd}_{0.6}\text{Sr}_{0.4}\text{Fe}_{0.8}\text{Al}_{0.2}\text{O}_{3-\delta}$ (CN-NSFA), which show comparable oxygen permeability and CO_2 resistance [29,39–42]. However, oxygen permeability is still not high enough to meet industrial requirements ($\geq 1 \text{ mL cm}^{-2} \text{ min}^{-1}$). Therefore, development of new dual-phase membranes with both high oxygen permeability and stability is still highly demanded.

Recently, Balagueret et al. has reported that transition metal cobalt doping into ceria-based oxides $\text{Ce}_{1-x}\text{Ln}_x\text{O}_{2-\delta}$ ($\text{Ln} = \text{Gd}, \text{La}, \text{Tb}, \text{Pr}, \text{Eu}, \text{Er}, \text{Yb}, \text{and Nd}$) can improve their total conductivity, and it is especially evident for Tb and Pr systems, which present remarkable improvements [43]. In addition, Fang et al. found that the electronic and ionic conductivity of $\text{Ce}_{0.85}\text{Gd}_{0.1}\text{Cu}_{0.05}\text{O}_{2-\delta}$ were improved by Cu doping and the obtained oxygen permeation membrane 75 wt.% $\text{Ce}_{0.85}\text{Gd}_{0.1}\text{Cu}_{0.05}\text{O}_{2-\delta}$ -25 wt.% $\text{La}_{0.6}\text{Ca}_{0.4}\text{FeO}_{3-\delta}$, which is composed of two mixed ionic electronic conductor phases and displays excellent oxygen permeability in the CO_2 atmosphere [44]. The aforementioned findings imply that adding metal transition metals such as Co or Cu into $\text{Ce}_{1-x}\text{Ln}_x\text{O}_{2-\delta}$ oxides can enhance the electronic and ionic conductivity and further improve the oxygen permeability. In fact, many metal oxides such as MnO_2 , MnO_3 , GaO_3 , Co_3O_4 , and Fe_2O_3 are considered to be able to improve the density because their melting point is much lower than those of lanthanide, meaning they also can act as sintering aids [45,46].

Currently, the 60 wt.% $\text{Ce}_{0.9}\text{Pr}_{0.1}\text{O}_{2-\delta}$ -40 wt.% $\text{Pr}_{0.6}\text{Sr}_{0.4}\text{FeO}_{3-\delta}$ (CP-PSF) membrane has been reported to yield $0.26 \text{ mL min}^{-1} \text{ cm}^{-2}$ oxygen permeation flux at $950 \text{ }^\circ\text{C}$ (with 0.5 mm thickness and He as sweeping gas) and has exhibited good stability in the partial oxidation of methane to syngas experiment [34]. More recently, we have designed $\text{Ce}_{0.9}\text{Pr}_{0.1}\text{O}_{2-\delta}$ - $\text{Pr}_{0.6}\text{Sr}_{0.4}\text{Fe}_{0.8}\text{Al}_{0.2}\text{O}_{3-\delta}$ (CP-PSFA) by doping Al in B-site of perovskite phase in CP-PSF and found higher oxygen permeability can be achieved [47]. Based on the above achievements, we further design a series of new dual-phase OTMs with the compositions of 60 wt.% $\text{Ce}_{0.85}\text{Pr}_{0.1}\text{M}_{0.05}\text{O}_{2-\delta}$ -40 wt.% $\text{Pr}_{0.6}\text{Sr}_{0.4}\text{Fe}_{0.8}\text{Al}_{0.2}\text{O}_{3-\delta}$ ($\text{M} = \text{Fe}, \text{Co}, \text{Ni}, \text{and Cu}$) (CPM-PSFA) and the oxygen permeability, as well as systematically studying stability. The aim of the work will focus on the study of the effect of doping Fe, Co, Ni, and Cu transition metals into CP phase on the oxygen permeability and stability.

2. Materials and Methods

2.1. Preparation of Powders and Membranes

The powders of 60 wt.%Ce_{0.85}Pr_{0.1}M_{0.05}O_{2-δ}-40 wt.%Pr_{0.6}Sr_{0.4}Fe_{0.8}Al_{0.2}O_{3-δ} (M = Fe, Co, Ni, and Cu) (CPM-PSFA) composites were obtained via a modified one-pot Pechini method. First, the corresponding nitrates on the basis of the stoichiometric ratio of the composites were weighted and formulated into a homogeneous aqueous solution. Subsequently, citric acid and ethylene glycol are added into the solution as a chelating agent and a surfactant, respectively. The molar mass ratio of the metal nitrate, citric acid, and ethylene glycol is 1:2:2. By heating and stirring the above solutions to evaporate the water and then turn it into viscous gels. Then, the air bakeout of these gels is carried out in an oven at around 150 °C, followed by crushing into the powder precursors. The ground precursors were first heated at 600 °C, then heated up to 950 °C, and kept at that temperature for 12 h in a muffle furnace. After these calcinations, we can get the target CPM-PSFA composite powders. Next, we put the pre-obtained composite powders into the stainless-steel mold with a diameter of 15 mm, added ~12 MPa pressure, and held it for around 5–10 min. The membrane embryos obtained from pressure are heated in air at 1275 °C for 5 h with an ascending and descending temperature rate of 1.5 °C/min. After the sintering process, we obtained the dense CPM-PSFA composite membranes. Finally, the membranes after sintering were carefully polished to a thickness of 0.6 mm with mesh sandpapers and then cleaned with absolute ethyl alcohol.

2.2. Characterization of Membranes

To exploit the phase purity and crystal structure of the 60 wt.%Ce_{0.85}Pr_{0.1}M_{0.05}O_{2-δ}-40 wt.%Pr_{0.6}Sr_{0.4}Fe_{0.8}Al_{0.2}O_{3-δ} (M = Fe, Co, Ni, and Cu) (CPM-PSFA) powders and membranes, we carried out the room temperature X-ray diffraction (XRD, D-MAX 2200 VPC, Rigaku with Cu K α) measurements. Moreover, we analyzed the room temperature XRD data by the Fullprof suite software with Rietveld refinement model. The lattice parameters are obtained by fitting the XRD patterns with Fullprof software (version: 14-June-2018). We further investigated the microscopic morphologies and chemical compositions of the sintered membranes by several characterizations including scanning electron microscopy (SEM, Quanta 400F, Oxford), energy dispersive X-ray spectroscopy (EDXS), and backscattered scanning electron microscopy (BSEM). Resistivity was measured by the physical property measurement system (PPMS) with the four-probe method.

2.3. Oxygen Permeability of Membranes

Oxygen permeation fluxes through the 60 wt.%Ce_{0.85}Pr_{0.1}M_{0.05}O_{2-δ}-40 wt.%Pr_{0.6}Sr_{0.4}Fe_{0.8}Al_{0.2}O_{3-δ} (M = Fe, Co, Ni, Cu) (CPM-PSFA) composite membranes were explored by a homemade high-temperature oxygen setup connected to a gas chromatograph (GC, Zhonghuida-A60, Dalian, China), as reported in the previous literatures [43,44]. Figure S4 shows our homemade high-temperature oxygen setup. As shown in Figure S4, the CPM-PSFA (M = Fe, Co, Ni, Cu) dual-phase membranes were glued on an alundum tube with the ceramic adhesive (Huitian 2767, China) and dried in air at 140 °C for 10 h. Then we put the corundum tube with a sealed dual-phase membrane inside a sealed quartz tube. Two ends of quartz tubes were fixed by brass nuts with O-ring. When the assembled membrane permeator were ready, we then loaded it into the tube muffle furnace and made sure the sealed dual-phase membrane sits on the middle of the muffle furnace. Generally speaking, the sealed membranes were assembled into the homemade high-temperature oxygen setup and then employed as the membrane separation reactor. After checking the gas tightness, the dry synthetic air with a flow rate of 100 cm³ min⁻¹ was inlet into one side of the sealed membrane; meanwhile He or CO₂ (49 cm³ min⁻¹) as the sweeping gases with Ne (1 cm³ min⁻¹) as a standard gas were inlet into the other side of the sealed membrane. All on-flow gas flows are regulated by the mass flowmeters (Sevenstar, China), which are made the periodic calibration with a soap membrane flow meter. The produced mixture gases were detected by an online connection GC with a 1000 mesh carbon molecular sieve.

The oxygen permeation rates through the composite membranes can be calculated on the basis of the following relationship [48].

$$J_{O_2} = \left(C_{O_2} - \frac{C_{N_2}}{4.02} \right) \times \frac{F_{Ne}^{inlet}}{S \times C_{Ne}^{outlet}} \quad (1)$$

C_{O_2} , C_{N_2} , and C_{Ne}^{outlet} are the percentages of oxygen, nitrogen, and neon in the outlet flow gas, and F_{Ne}^{inlet} is the flow rate of neon gas when it flows into the sweep side (the neon gas flow rate is 1 mL min^{-1}). S represents the effective penetrating areas of the CPM-PSFA (M = Fe, Co, Ni, and Cu) ceramic composite membranes sealed on the aluminum tube.

In addition, 4.02 is calculated from the relation $\frac{C_{N_2}^{leak}}{C_{O_2}^{leak}} = \sqrt{\frac{32}{28}} \times \frac{79\%}{21\%} = 4.02$ (where $C_{O_2}^{leak}$ and $C_{N_2}^{leak}$ are the leaked oxygen and leaked nitrogen content, respectively; 32 and 28 are the molar masses of nitrogen and oxygen, respectively; 79 and 21% correspond to the proportion of nitrogen and oxygen in the air, respectively) and denotes the ratio of the leaked nitrogen on the basis of the theory of Kundsens diffusion. When we calculated the real permeation fluxes through our membranes, the subtle air diffusion through the ceramic adhesive should be taken into consideration and thereby the oxygen from the leakage of the seal should be subtracted.

3. Results and Discussion

3.1. Structural Characterization

Figure 1 manifests the room-temperature XRD patterns of the CPM-PSFA (M = Fe, Co, Ni, Cu) composite powders after heated in air at $950 \text{ }^\circ\text{C}$ for 10 h. From Figure 1, we can see that the XRD peaks are assigned to the fluorite phase CPM and the perovskite phase PSFA; there is no other impurity phase can be found. Moreover, it can be observed that after doping Fe, Co, Ni, and Cu transition metal elements into CP-PSFA, there is no shift for the peak of PSFA phase, while the peak of fluorite phase has shifted towards high angles, suggesting that these Cu, Co, Fe, and Ni transition metal elements have been successfully doped into only the fluorite phase (CP) but not the perovskite phase (PSFA). These results indicate that the CPM-PSFA dual-phase powders had been successfully prepared via the modified one-pot Pechini method. No obvious reaction or diffusion between the two phases can be detected within our XRD resolution limit.

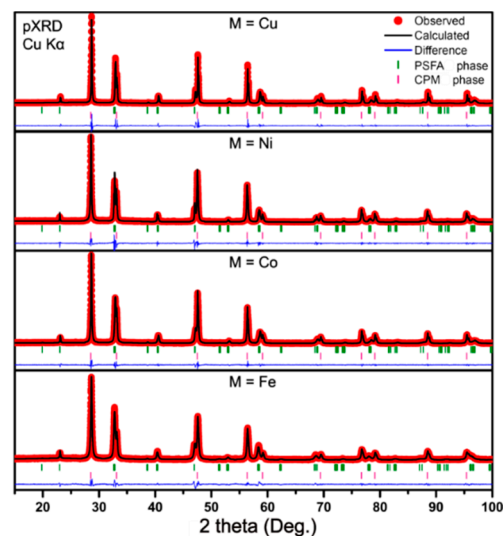


Figure 1. X-ray powder diffraction (XRD) refinements for CPM-PSFA (M = Fe, Co, Ni, Cu) powders after calcined at $950 \text{ }^\circ\text{C}$ for 10 h in air, respectively.

To exploit the phase purity and structure of the composite membranes, we also use the room-temperature XRD to characterize the sintered membranes (Figures S1–S3). Figures S1–S3 show the XRD patterns for the CPM-PSFA (M = Fe, Co, Ni, Cu) dual-phase membranes after sintering at 1275 °C, 1350 °C, and 1400 °C for 5 h, respectively. As shown in Figures S1–S3, all these sintered membranes also consist of CPM and PSFA two phases. No other impurities can be observed. XRD results imply that all four sintered composite membranes that were studied kept the same structures as the powders, suggesting the sintered CPM-PSFA composite membranes were prepared successfully. Moreover, we further perform XRD refinements for all the dual-phase powders obtained by heating at 950 °C for 10 h using the Rietveld model to get more information in detailed. The obtained cell parameters are listed in Table 1. There is hardly change in the cell parameters of PSFA phase from the CPM-PSFA composite, whereas the cell parameters of CPM phase significantly decreased compared with that of the undoped fluorite phase (CP). The shrinking lattice parameters in CPM (M = Fe, Co, Ni, and Cu) are all smaller than that of the undoped CP because of the smaller ion radius of Fe³⁺ (0.0645 nm), Co²⁺ (0.0745 nm), Ni²⁺ (0.056 nm), and Cu²⁺ (0.073 nm) compared with that of Ce⁴⁺ (0.087 nm). In other words, since ionic radius of these dopants (Cu²⁺, Co²⁺, Fe³⁺, and Ni²⁺) is smaller than that of Ce⁴⁺, the lattice constant *a* in CPM is expected to be smaller than that of the pristine CP, further implying that these transition metal elements have been successfully substituted into CP phase instead of PSFA phase.

Table 1. Unit cell parameters of CPM-PSFA powders obtained by heating at 950 °C for 10 h.

Materials	CP	PSFA (t = 0.86195)		
	a = b = c (Å)	a (Å)	b (Å)	c (Å)
CPFe-PSFA	5.4100 (3)	5.4419 (4)	7.7355 (3)	5.4848 (4)
CPCo-PSFA	5.4099 (3)	5.4415 (3)	7.7358 (2)	5.4842 (3)
CPNi-PSFA	5.4099 (4)	5.4413 (3)	7.735 (3)	5.4845 (3)
CPCu-PSFA	5.4102 (3)	5.4416 (2)	7.7359 (4)	5.4844 (4)
CP-PSFA ¹	5.4131 (3)	5.4414 (3)	7.7356 (3)	5.4844 (4)

¹ The data is from ref. [33].

3.2. Morphology Characterization

To check the density of the sintered membranes before being used for the oxygen permeability test, SEM is employed to characterize the microscopic morphology of the CPM-PSFA (M = Fe, Co, Ni, Cu) membranes. After several sintering temperature attempts, we finally found out that the appropriate sintering temperature for the CPM-PSFA (M = Fe, Co, Ni, Cu) composite membranes is in the temperature range of 1250–1300 °C. Compared with the sintering temperature of undoped CP-PSFA (1450–1500 °C, 5 h), the sintering temperature for CPM-PSFA can be remarkably reduced after adding the transition metals (M = Fe, Co, Ni, and Cu) into the fluorite phase being as the sintering aids. The significant reduction of sintering temperature is not only in favor of the reduction of the energy consumption in the material preparation process but also the requirements for equipment. Here, for better comparison, we adopt the final sintering temperature at 1275 °C for 5 h for all the samples. As presented in Figure 2, there are no cracks or interlocking pores on the surfaces of these composite membranes after sintering in air at 1275 °C for 5 h, indicating that all these sintered membranes were dense. In addition, the backscattered scanning electron microscope (BSEM) images can be distinguished by two different colors, which indicates that the sintered membranes are mainly composed of two phases. The bright region represents the CPM phase and the dark region represents the PSFA phase due to the increase of the strength of backscattered electron signal with the increase of atomic number. Moreover, it is obvious that the grain sizes of the CPM phase and PSFA phase are very similar. In addition, the copper-doping membrane CPCu-PSFA obviously displays the largest grain size of the other three membranes. Two phases are evenly distributed in the membranes and form the percolated paths, which play an important part in the

migration of the electron and oxygen ions during the process of oxygen permeation. The percolation network between OIC and IC phase ensures that electron and oxygen ions can smoothly diffuse from one side to another side of the membrane driven by chemical potential difference, so as to realize the high oxygen permeability. Therefore, we have reason to expect that CPM-PSFA OTMs will show considerable flux in the following oxygen permeation test.

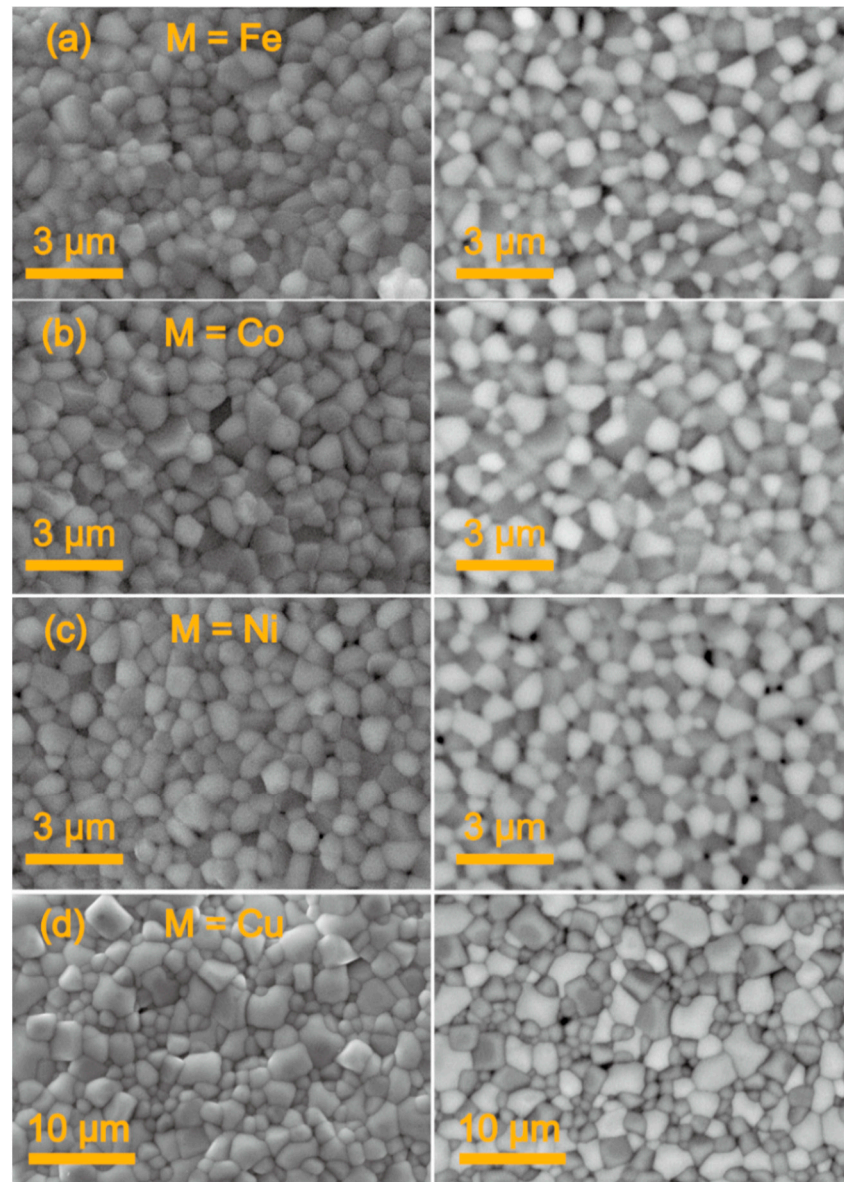


Figure 2. Surface topographies of (a) CPFe-PSFA, (b) CPCo-PSFA, (c) CPNi-PSFA, and (d) CPCu-PSFA. Left column is SEM and right column is backscattered scanning electron microscope (BSEM) pictures for the sintered membranes. In BSEM, the perovskite phase (PSFA) grains are in dark color; the CPM grains are in light color.

Figure 3 depicts the EDXS pictures and element mappings for our four CPM-PSFA composite membranes after sintering at 1275 °C for 5 h. We can see that two phases form a well-interpenetrated network, which provides the percolation paths for the oxygen permeation. Correspondingly, the Cu-doping membrane CPCu-PSFA shows the biggest grain size among these four membranes, which may play a positive role in the oxygen flux. This self-adjusting of composites between two phases may be attributed to the diverse chemical potential of elements in PSFA and CPM phases.

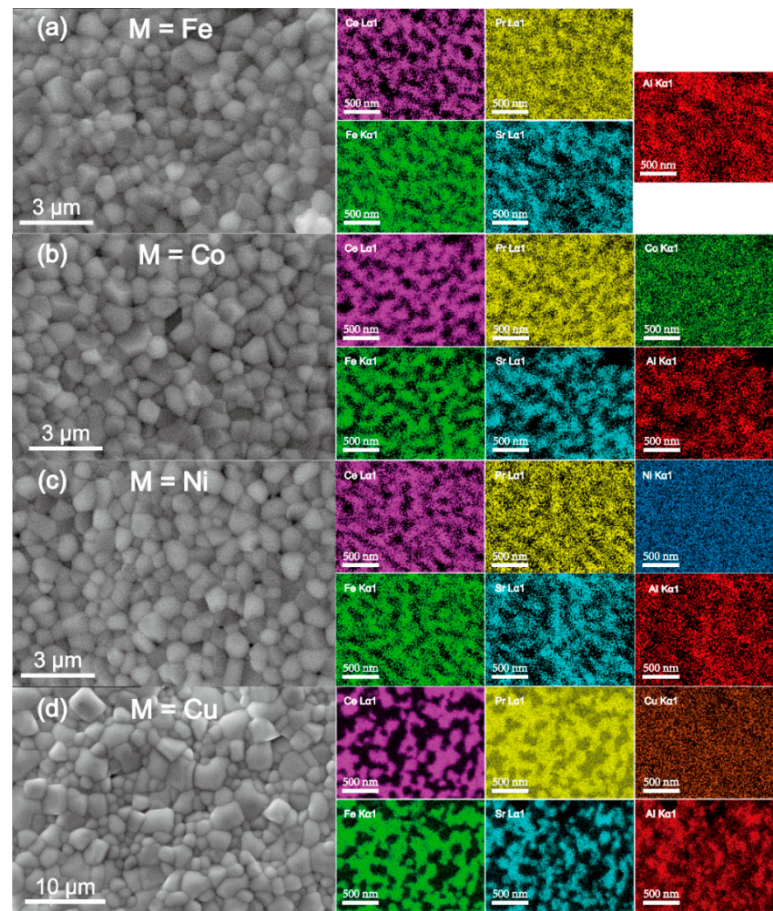


Figure 3. EDXS and element mapping images for (a) CPFe-PSFA, (b) CPCo-PSFA, (c) CPNi-PSFA, and (d) CPCu-PSFA composite membranes after sintering at 1275 °C for 5 h.

Next, we study the effect of the sintering acids on the oxygen permeability through the CPM-PSFA OTMs. From Figure 4a, it can be seen that the oxygen permeation rates through all the CPM-PSFA OTMs increase with the increment of measuring temperature. It is worth noting that the dual-phase membranes doped with Cu and Co into the fluorite phase CP show higher oxygen permeability than that of the pristine CP-PSFA membrane under the similar operation condition. The 0.6 mm-thickness CPCu-PSFA membrane exhibits a $1.05 \text{ mL min}^{-1} \text{ cm}^{-2}$ oxygen permeation rate at 1000 °C when using helium as sweep gas, which reaches the minimum value of oxygen permeation rate ($1 \text{ mL min}^{-1} \text{ cm}^{-2}$) requirement for the application of oxygen permeable membranes in industry [49]. In addition, the oxygen permeation rate through the CPCo-PSFA membrane reaches $0.87 \text{ mL min}^{-1} \text{ cm}^{-2}$ at 1000 °C, which is 13% higher than that of CP-PSFA. However, there is a subtle increase of the oxygen permeation rates through the CPNi-PSFA and CPFe-PSFA composite membranes in comparison with that of CP-PSFA membrane (see Figure 5). The above results indicate that the doping of Cu and Co has a positive effect on the oxygen permeability of the CP-PSFA-based membranes. This positive effect may be ascribed to the partial substitution of Ce^{4+} by lower valent Cu^{2+} and Co^{2+} , which provide more oxygen vacancies for CP. On the other hand, we have used the physical property measurement system (PPMS) to measure the resistivity in the 275 K–350 K of our 60 wt.% $\text{Ce}_{0.85}\text{Pr}_{0.1}\text{M}_{0.05}\text{O}_{2-\delta}$ -40 wt.% $\text{Pr}_{0.6}\text{Sr}_{0.4}\text{Fe}_{0.8}\text{Al}_{0.2}\text{O}_{3-\delta}$ (M = Fe, Co, Ni, Cu) (CPM-PSFA) samples. The results are shown in Figure S5 in our revised manuscript. In addition, the calculated electronic conductivity of CPM-PSFA (M = Fe, Co, Ni, Cu) at 350 K are $0.11499 \text{ S}\cdot\text{cm}^{-1}$, $0.2172 \text{ S}\cdot\text{cm}^{-1}$, $0.11448 \text{ S}\cdot\text{cm}^{-1}$, and $0.23083 \text{ S}\cdot\text{cm}^{-1}$. Among them, CPCu-PSFA shows the highest conductivity at 350 K, followed by the CPCo-PSFA. Thus, the doping of Cu^{2+} and Co^{2+} provides a certain electronic conductivity for CP, which means that the materials consist of two

mixed-conducting phases, i.e., both fluorite phase and perovskite phase can conduct both oxygen ions and electrons, thus making the membrane exhibit better oxygen permeability. At the same time, we compare the average grain sizes of the CPM-PSFA (M = Fe, Co, Ni, and Cu) composite membranes after sintering at 1275 °C in Table S2. We find that the average grain size for CPCu-PSFA is the largest, followed by the system doped with Co element among these four dual-phase membranes. It seems like that the large grain size has a positive effect on the oxygen permeation flux in our studied dual-phase membranes, which is similar to the findings in some single-type oxygen permeable membranes [50,51].

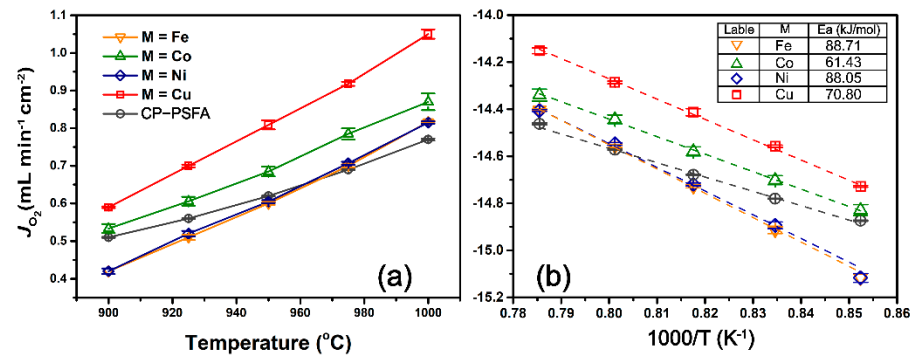


Figure 4. (a) Oxygen permeation rates through the CPMPSFA (M = Fe, Co, Ni, Cu) composite membranes. (b) Arrhenius plot of oxygen permeation rates for CPM-PSFA (M = Fe, Co, Ni, and Cu) composite membranes. Condition: 150 mL min⁻¹ air as the feed gas, 49 mL min⁻¹ He as the sweep gas, 1 mL min⁻¹ Ne as an internal standard gas. Membrane thickness: 0.6 mm.

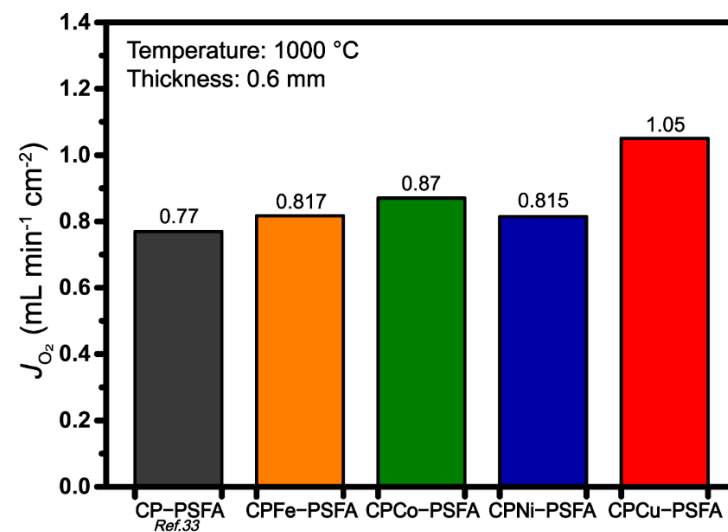


Figure 5. Comparison of oxygen permeation rates through the CPM-PSFA (M = Fe, Co, Ni, and Cu) composite membranes at 1000 °C. Condition: 150 mL min⁻¹ air as the feed gas, 49 mL min⁻¹ He as the sweep gas, and 1 mL min⁻¹ Ne as an internal standard gas. Membrane thickness: 0.6 mm.

In addition, to study the activation energy of oxygen in the process of permeation, we draw Arrhenius plots based on the relationship between temperature and oxygen permeation rates (Figure 4b). The apparent activation energy of CPM-PSFA (M = Fe, Co, Ni, and Cu) were 88.71, 61.43, 88.05, and 70.80 kJ mol⁻¹, respectively. The CPCu-PSFA oxygen permeable membrane exhibits the smallest activation energy, and the calculation shows that it has the largest pre-exponential factor, which means that the membrane doped with copper has the most reaction sites for interface exchange process among these studied membranes. In order to further explore the effect of Fe, Co, Ni, and Cu doping on fluorite

phase, we calculated the ionic conductivity of 0.6 mm-thickness CPM-PSFA membrane at 1273.15 K according to the Wagner equation: [52]

$$J_{O_2} = \frac{RT}{16F^2L} \int_{\ln P_1}^{\ln P_2} \frac{\sigma_{ion}\sigma_e}{\sigma_{ion} + \sigma_e} d(\ln P_0) \quad (2)$$

Considering that in dual-phase mixed-conducting OTM, electronic conductivity is often much larger than ionic conductivity ($\sigma_e \gg \sigma_i$) making the equation approximately to be as follows:

$$J_{O_2} \cdot L = -\frac{RT}{16F^2} \int_{\ln p'_{O_2}}^{\ln p''_{O_2}} \sigma_i d \ln p_{O_2} \quad (3)$$

The calculated ionic conductivity of CPM-PSFA (M = Fe, Co, Ni, Cu) are 0.0182, 0.0194, 0.0181, and 0.0243 S·cm⁻¹, respectively, which are higher than that of CP-PSFA (0.0179 S·cm⁻¹). This indicates that the oxygen vacancies in CPM phase are enhanced due to the low-valence of transition metal oxygen ions, thus exhibiting better ionic conductivity.

Table 2 shows the comparison of oxygen permeation fluxes of different oxygen permeable membranes. As shown in Table 2, we can see that our dual-phase membranes have lower oxygen permeability than that of co-based SrSc_{0.05}Co_{0.95}O_{3-δ} single perovskite membrane [53] but have near double higher [33,54] or comparable oxygen permeability compared with other dual-phase membranes [55,56]. To further benchmark the potential practical application of OTMs in oxy-fuel combustion, one of the important factors is whether the OTM can operate stably in rich carbon dioxide atmospheres at high temperature. So far, most of the previous findings on the single-phase perovskite (ABO₃) membranes adopted alkali-earth elements in A or B site. This leads to the formation of carbonates in CO₂ rich atmosphere at high temperature and the stop of oxygen permeation [57]. Thus, it is necessary to check the stability for our CPM-PSFA membranes under low oxygen atmosphere. Figure 6a,b shows the in situ XRD patterns for the CPCu-PSFA and CPCo-PSFA materials from 30 to 1000 °C. In situ XRD patterns show that there is no carbonates or other impurity phase that can be observed in the CPCu-PSFA and CPCo-PSFA composites in the range of 30 to 1000 °C, indicating they are stable in pure CO₂ condition. Moreover, Figure 6c,d shows the XRD patterns for the CPNi-PSFA and CPFe-PSFA composites after treating in pure CO₂ condition at several temperatures (200 °C, 400 °C, 600 °C, 800 °C, and 1000 °C) for 24 h. As shown in Figure 6c,d, all these composites also maintain fluorite and perovskite two phases, and neither carbonates nor other impurity can be found. Collectively, all these four studied compounds are phase stable in pure CO₂ atmosphere.

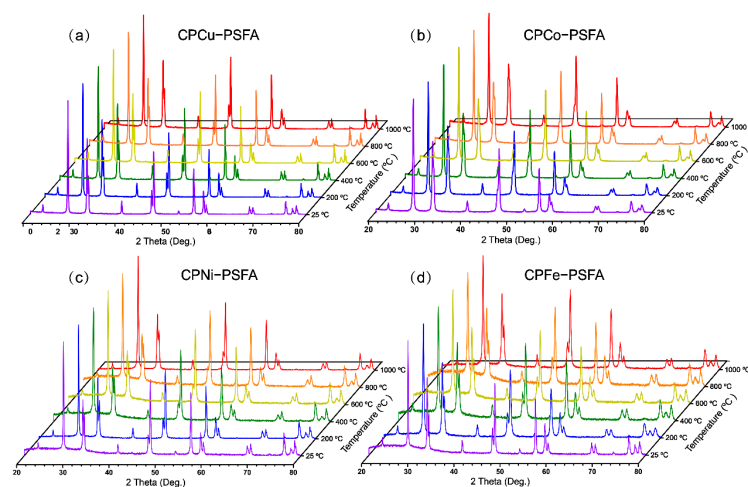


Figure 6. In-situ XRD patterns for (a) CPCu-PSFA and (b) CPCo-PSFA powders under CO₂ atmosphere in the temperature range of 25–1000 °C; XRD patterns of (c) CPNi-PSFA and (d) CPFe-PSFA powders calcined at 25–1000 °C for 24 h under CO₂ atmosphere.

Table 2. Comparison of oxygen permeation fluxes of different oxygen permeable membranes.

Materials	Thickness (mm)	Temperature (°C)	J_{O_2} (mL cm ⁻² min ⁻¹) (Sweeping Gas: He)	Ref.
SrSc _{0.05} Co _{0.95} O _{3-δ}	0.91	900	3.10	[53]
Ce _{0.85} Sm _{0.15} O _{1.925-}	0.5	950	0.50	[54]
Sm _{0.6} Sr _{0.4} Al _{0.3} Fe _{0.7} O _{3-δ}				
60 wt.%Ce _{0.9} Pr _{0.1} O _{2-δ-}	0.6	1000	1.08	[55,58]
40 wt.%Pr _{0.6} Sr _{0.4} Fe _{0.5} Co _{0.5} O _{3-δ}				
60 wt.%Ce _{0.8} Nd _{0.2} O _{2-δ-}	0.6	1000	1.00	[55,56]
40 wt.%Nd _{0.5} Sr _{0.5} Al _{0.2} Fe _{0.8} O _{3-δ}				
60 wt.%Ce _{0.9} Pr _{0.1} O _{2-δ-}	0.6	1000	0.77	[33]
40 wt.%Pr _{0.6} Sr _{0.4} Fe _{1-x} Al _x O _{3-δ}				
60 wt.%Ce _{0.85} Pr _{0.1} Fe _{0.05} O _{2-δ-}	0.6	1000	0.82	This work
40 wt.%Pr _{0.6} Sr _{0.4} Fe _{0.8} Al _{0.2} O _{3-δ}				
60 wt.%Ce _{0.85} Pr _{0.1} Co _{0.05} O _{2-δ-}	0.6	1000	0.87	This work
40 wt.%Pr _{0.6} Sr _{0.4} Fe _{0.8} Al _{0.2} O _{3-δ}				
60 wt.%Ce _{0.85} Pr _{0.1} Ni _{0.05} O _{2-δ-}	0.6	1000	0.82	This work
40 wt.%Pr _{0.6} Sr _{0.4} Fe _{0.8} Al _{0.2} O _{3-δ}				
60 wt.%Ce _{0.85} Pr _{0.1} Cu _{0.05} O _{2-δ-}	0.6	1000	1.05	This work
40 wt.%Pr _{0.6} Sr _{0.4} Fe _{0.8} Al _{0.2} O _{3-δ}				

Subsequently, we carried out the long-time oxygen permeability test for the optimal CPCu-PSFA membrane in the range of 900–1000 °C. Encouragingly, CPCu-PSFA composite membrane still maintains both high oxygen flux and acceptable stability in CO₂ environment. As illustrated in Figure 7, during the first 40 h of the test, the oxygen permeability increases with the increase of temperature. When the temperature is stable at 1000 °C, the J_{O_2} also stabilizes at the level of about 1.05 mL min⁻¹ cm⁻². When the sweep gas is changed from He to CO₂, the oxygen permeation flux decreases first in a cliff-like manner, because the adsorption of CO₂ reduces the surface exchange rate of O₂. Similar phenomena have been reported in other reports [59,60]. Then, the oxygen permeation rate remains unchanged at about 0.72 mL min⁻¹ cm⁻² until the temperature begins to drop. In the end, the CPCu-PSFA membrane works stably in CO₂ environment for 100 h until we stopped the test. Moreover, XRD analysis was performed on all CPM-PSFA membranes after oxygen permeability. As shown in Figure 8, no impurities are found in the CPM-PSFA membranes after long-term oxygen permeability test. In general, CPM-PSFA membranes not only exhibit excellent oxygen permeability but also exhibit good CO₂-tolerance stability, which makes it possible for further application in the oxy-fuel process.

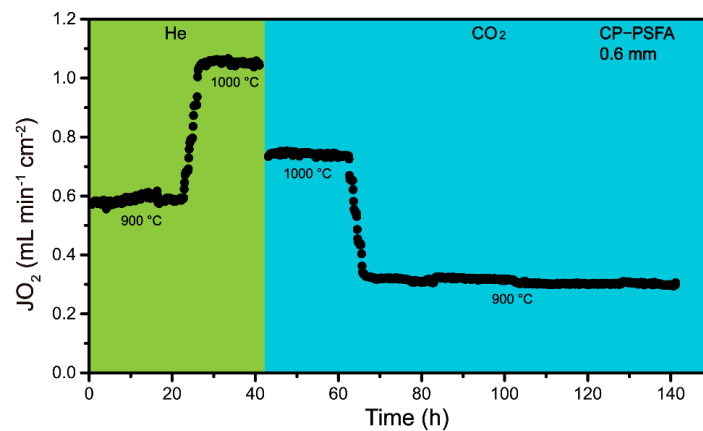


Figure 7. Oxygen permeation fluxes of CPCu-PSFA membrane as a function of time. Condition: 150 mL min⁻¹ air as the feed gas, 49 mL min⁻¹ He and CO₂ as the sweep gas, and 1 mL min⁻¹ Ne as an internal standard gas. Membrane thickness: 0.6 mm.

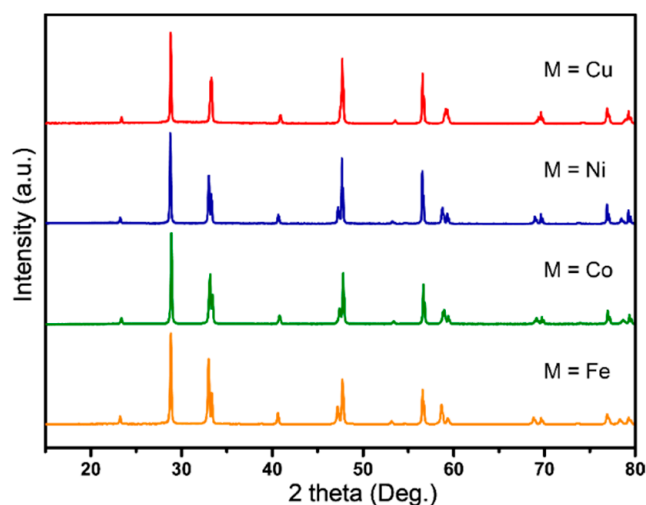


Figure 8. XRD patterns of the spent CPM-PSFA (M = Fe, Co, Ni, Cu) membranes after oxygen permeability test, respectively.

4. Conclusions

The successful synthesis of CPM-PSFA proves that the modified Pechini method is suitable and effective for the synthesis of oxygen permeation membranes. XRD and BSEM morphologies reveal that the obtained composite compounds consist of fluorite phase and perovskite phase, and Cu, Co, Fe, and Ni are successfully doped into fluorite phase (CPO), which makes the fluorite phase change from a pure ionic conductor to mixed ionic electronic conductor. It is precisely because CPM-PSFA membrane consists of two mixed ion electronically conductive phases, and the surface of the membrane is densely distributed in two phases, and the ions and electrons have a continuous channel in both phases, meaning the oxygen permeable membrane exhibits high oxygen permeability. Among them, the oxygen permeability through CPCu-PSFA and CPCo-PSFA composites has been further improved compared with that of the parent CP-PSFA. XRD and long-term oxygen permeability tests show that CPM-PSFA composites maintain excellent phase stability and oxygen permeation stability. A series of oxygen permeable membranes CP-PSF, CP-PSFA, and CPM-PSFA have been successfully synthesized and their oxygen permeability has been gradually increased, which proves our success in improving oxygen permeability of oxygen permeable membranes and ensuring high stability of oxygen permeable membranes. This work can provide a reference for further design and synthesis of other new oxygen permeable membrane materials, and the oxygen permeable membranes studied in this work have great potential application prospects in the field of oxygen separation and oxy-fuel combustion.

Supplementary Materials: The following are available online at <https://www.mdpi.com/2227-9717/9/3/528/s1>, Table S1: the relative density of CPM-PSFA (M = Fe, Co, Ni, Cu) composite membranes after sintering at 1275 °C. Table S2: the average grain size of CPM-PSFA (M = Fe, Co, Ni, Cu) composite membranes after sintering at 1275 °C for 5 h. Figures S1–S3: XRD patterns of CPM-PSFA (M = Fe, Co, Ni, Cu) membranes after sintering at 1275 °C, 1350 °C and 1400 °C for 5 h before oxygen permeability test, respectively. Figure S4: schematic diagram of oxygen permeability test device. Figure S5 (a) The temperature dependence of resistivity of the CPM-PSFA (M = Fe, Co, Ni, Cu) in the 275K–350K. (b) temperature dependence of conductivity of CPM-PSFA (M = Fe, Co, Ni, Cu) in the 275 K–350 K.

Author Contributions: H.L., X.W. and L.S. conceived and designed the experiments; X.W. and L.S. prepared the samples and the oxygen permeation test; Y.H. did the phase stability test under Ar atmosphere; L.Z. and M.B. did the XRD, SEM and BSEM analysis; D.L. assisted to prepare the samples; X.W., L.S. and H.L. analyzed all the data and wrote the paper. All authors have read and agreed to the published version of the manuscript.

Funding: This research was funded by the National Natural Science Foundation of China (Grants No. 11922415), Guangdong Basic and Applied Basic Research Foundation (2019A1515011718), the Fundamental Research Funds for the Central Universities (19lgzd03), Key Research and Development Program of Guangdong Province, China (2019B110209003), and the Pearl River Scholarship Program of Guangdong Province Universities and Colleges (20191001).

Institutional Review Board Statement: Not applicable.

Informed Consent Statement: Not applicable.

Data Availability Statement: The study did not report any data.

Acknowledgments: We acknowledge for S. Wang for useful discussions.

Conflicts of Interest: The authors declare no conflict of interest.

References

1. Wei, Y.Y.; Tang, J.; Zhou, L.Y.; Li, Z.; Wang, H.H. Oxygen permeation through U-shaped K_2NiF_4 —Type oxide hollow-fiber membranes. *Ind. Eng. Chem. Res.* **2011**, *50*, 12727–12734. [[CrossRef](#)]
2. Wei, Y.Y.; Liao, Q.; Xue, J.; Li, Z.; Wang, H.H. Influence of SO_2 on the phase structure, oxygen permeation and microstructure of K_2NiF_4 —type hollow fiber membranes. *Chem. Eng. J.* **2013**, *217*, 34–40. [[CrossRef](#)]
3. Liu, Y.; Zhu, X.F.; Li, M.R.; O’Hayre, R.P.; Yang, W.S. Nanoparticles at grain boundaries inhibit the phase transition of perovskite membrane. *Nano Lett.* **2015**, *15*, 7678–7683. [[CrossRef](#)]
4. Du, Z.H.; Ma, Y.H.; Zhao, H.; Kui Li, Y.L. High CO_2 -tolerant and Cobalt-free dual-phase membranes for pure oxygen separation. *J. Membr. Sci.* **2019**, *574*, 243–251. [[CrossRef](#)]
5. Lee, S.I.; Choi, M.B.; Dasari, H.P.; Hong, J.; Kim, H.C.; Son, J.W.; Lee, J.H.; Kim, B.K.; Je, H.J.; Yoon, K.J. Role of ceria-Zirconia solid solution with high oxygen storage capacity in cermet anodes of solid oxide fuel cells. *J. Electrochem. Soc.* **2014**, *161*, F883–F888. [[CrossRef](#)]
6. Liang, W.Y.; Zhou, H.Y.; Caro, J.; Jiang, H.Q. Methane conversion to syngas and hydrogen in a dual phase $Ce_{0.8}Sm_{0.2}O_{2-\delta}$ - $Sr_2Fe_{1.5}Mo_{0.5}O_{5+\delta}$ membrane reactor with improved stability. *Int. J. Hydrog. Energy* **2018**, *43*, 14478–14485. [[CrossRef](#)]
7. Tonziello, J.; Vellini, M. Oxygen production technologies for IGCC power plants with CO_2 capture. *Energy Procedia* **2011**, *4*, 637–644. [[CrossRef](#)]
8. Lima, F.; Daoutidis, P.; Tsapatsis, M. Modeling, optimization, and cost analysis of an IGCC plant with a membrane reactor for carbon capture. *AIChE J.* **2016**, *62*, 1568–1580. [[CrossRef](#)]
9. Dong, X.L.; Jin, W.Q.; Xu, N.P.; Li, K. Dense ceramic catalytic membranes and membrane reactors for energy and environmental applications. *Chem. Commun.* **2011**, *47*, 10886–10902. [[CrossRef](#)] [[PubMed](#)]
10. Cao, Z.W.; Jiang, H.Q.; Luo, H.X.; Baumann, S.; Meulenberg, W.A.; Assmann, J.; Mleczko, L.; Liu, Y.; Caro, J. Natural gas to fuels and chemicals: Improved methane aromatization in an oxygen-permeable membrane reactor. *Angew. Chem. Int. Ed.* **2013**, *52*, 13794–13797. [[CrossRef](#)] [[PubMed](#)]
11. Jiang, H.Q.; Wang, H.H.; Werth, S.; Schiestel, T.; Caro, J. Simultaneous production of hydrogen and synthesis gas by combining water splitting with partial oxidation of methane in a hollow-fiber membrane reactor. *Angew. Chem. Int. Ed.* **2008**, *47*, 9341–9344. [[CrossRef](#)]
12. Zhu, X.F.; Yang, W.S. Microstructural and interfacial designs of oxygen-permeable membranes for oxygen separation and reaction–separation coupling. *Adv. Mater.* **2019**, *31*, 1902547. [[CrossRef](#)]
13. Jiang, H.Q.; Wang, H.H.; Liang, F.Y.; Werth, S.; Schirmeister, S.; Schiestel, T.; Caro, J. Improved water dissociation and nitrous oxide decomposition by in situ oxygen removal in perovskite catalytic membrane reactor. *Catal. Today* **2010**, *156*, 187–190. [[CrossRef](#)]
14. Cai, L.L.; Zhu, Y.; Cao, Z.W.; Li, W.P.; Li, H.B.; Zhu, X.F.; Yang, W.S. Non-noble metal catalysts coated on oxygen-permeable membrane reactors for hydrogen separation. *J. Membr. Sci.* **2020**, *594*, 117463. [[CrossRef](#)]
15. Escolastico, S.; Solís, C.; Kjølseth, C.; Serra, J.M. Outstanding hydrogen permeation through CO_2 -stable dual-phase ceramic membranes. *Energy Environ. Sci.* **2014**, *7*, 3736–3746. [[CrossRef](#)]
16. Wu, X.Y.; Cai, L.L.; Zhu, X.F.; Ghoniem, A.F.; Yang, W.S. A high-efficiency novel IGCC-OTM carbon capture power plant design. *J. Adv. Manuf. Process.* **2020**, *2*, e10059. [[CrossRef](#)]
17. Maas, P.; Nauels, N.; Zhao, L.; Markewitz, P.; Scherer, V.; Modigell, M.; Stolten, D.; Hake, J.F. Energetic and economic evaluation of membrane-based carbon capture routes for power plant processes. *Int. J. Greenh. Gas Control* **2016**, *44*, 124–139. [[CrossRef](#)]
18. Chi, J.L.; Li, K.Y.; Zhang, S.J.; Zhu, X.F.; Zhao, L.F.; Wang, B.; Xiao, Y.H. Process simulation and integration of IGCC systems with novel mixed ionic and electronic conducting membrane-based water gas shift membrane reactors for CO_2 capture. *Int. J. Hydrog. Energy* **2020**, *45*, 13884–13898. [[CrossRef](#)]
19. Stadler, H.; Beggel, F.; Habermehl, M.; Persigehl, B.; Kneer, R.; Modigell, M.; Jeschke, P. Oxyfuel coal combustion by efficient integration of oxygen transport membranes. *Int. J. Greenh. Gas Control* **2011**, *5*, 7–15. [[CrossRef](#)]

20. Kim, J.S.; Lin, Y.S. Synthesis and oxygen-permeation properties of thin YSZ/Pd composite membranes. *AIChE J.* **2000**, *46*, 1521–1529. [[CrossRef](#)]
21. Han, N.; Wei, Q.; Tian, H.; Zhang, S.G.; Zhu, Z.H.; Liu, J.; Liu, S.M. Highly stable dual-phase membrane based on $\text{Ce}_{0.9}\text{Gd}_{0.1}\text{O}_{2-\delta}$ - $\text{La}_2\text{NiO}_{4+\delta}$ for oxygen permeation under pure CO_2 atmosphere. *Energy Tech.* **2019**, *7*, 1800701. [[CrossRef](#)]
22. Liu, T.; He, W.; Huang, H.; Wang, S.W.; Bouwmeester, H.J.M.; Chen, C.S. $\text{Ce}_{0.8}\text{Sm}_{0.2}\text{O}_{1.9}$ - $\text{La}_{0.8}\text{Sr}_{0.2}\text{Cr}_{0.5}\text{Fe}_{0.5}\text{O}_{3-\delta}$ dual-phase hollow fiber membranes operated under different gradients. *Ind. Eng. Chem. Res.* **2014**, *53*, 6131–6136. [[CrossRef](#)]
23. Lia, C.Q.; Ban, X.K.; Chen, C.S.; Zhan, Z.L. Sandwich-like symmetric dual-phase composite membrane with an ultra-thin oxygen separation layer and excellent durability. *Solid State Ion.* **2020**, *345*, 115176. [[CrossRef](#)]
24. He, W.; Liu, J.J.; Chen, C.S.; Ni, M. Oxygen permeation modeling for $\text{Zr}_{0.84}\text{Y}_{0.16}\text{O}_{1.92}$ - $\text{La}_{0.8}\text{Sr}_{0.2}\text{Cr}_{0.5}\text{Fe}_{0.5}\text{O}_{3-\delta}$ asymmetric membrane made by phase-inversion. *J. Membr. Sci.* **2015**, *491*, 90–98. [[CrossRef](#)]
25. Zhang, Z.C.; Ning, K.; Xu, Z.; Zheng, Q.K.; Tan, J.K.; Liu, Z.K.; Wu, Z.T.; Zhang, G.R.; Jin, W.Q. Highly efficient preparation of $\text{Ce}_{0.8}\text{Sm}_{0.2}\text{O}_{2-\delta}$ - $\text{SrCo}_{0.9}\text{Nb}_{0.1}\text{O}_{3-\delta}$ dual-phase four-channel hollow fiber membrane via one-step thermal processing approach. *J. Membr. Sci.* **2021**, *620*, 118752. [[CrossRef](#)]
26. Nam, G.D.; Lee, G.; Choi, S.; Lee, J.; Song, S.J.; Joo, J.H. A chemically and mechanically stable dual-phase membrane with high oxygen permeation flux. *J. Mater. Chem. A* **2020**, *8*, 23884–23893. [[CrossRef](#)]
27. Chen, G.X.; Tang, B.J.; Widenmeyer, M.; Wang, L.; Feldhoff, A.; Weidenkaff, A. Novel CO_2 -tolerant dual-phase $\text{Ce}_{0.9}\text{Pr}_{0.1}\text{O}_{2-\delta}$ - $\text{La}_{0.5}\text{Sr}_{0.5}\text{Fe}_{0.9}\text{Cu}_{0.1}\text{O}_{3-\delta}$ membranes with high oxygen permeability. *J. Membr. Sci.* **2020**, *595*, 117530. [[CrossRef](#)]
28. Xue, J.; Zheng, Q.; Wei, Y.Y.; Yuan, K.J.; Li, Z.; Wang, H.H. Dual phase composite oxide of $\text{Ce}_{0.9}\text{Gd}_{0.1}\text{O}_{2-\delta}$ - $\text{Ba}_{0.5}\text{Sr}_{0.5}\text{Co}_{0.8}\text{Fe}_{0.2}\text{O}_{3-\delta}$ with excellent oxygen permeation. *Ind. Eng. Chem. Res.* **2012**, *51*, 4703–4709. [[CrossRef](#)]
29. Luo, H.X.; Efimov, K.; Jiang, H.Q.; Feldhoff, A.; Wang, H.H.; Caro, J. CO_2 -stable and cobalt-free dual-phase membrane for oxygen separation. *Angew. Chem. Int. Ed.* **2011**, *50*, 759–763. [[CrossRef](#)]
30. Zhu, X.F.; Liu, H.Y.; Cong, Y.; Yang, W.S. Novel dual-phase membranes for CO_2 capture via an oxyfuel route. *Chem Commun.* **2012**, *48*, 251–253. [[CrossRef](#)]
31. Cai, L.L.; Hu, S.Q.; Cao, Z.W.; Li, H.B.; Zhu, X.F.; Yang, W.S. Dual-phase membrane reactor for hydrogen separation with high tolerance to CO_2 and H_2S impurities. *AIChE J.* **2019**, *65*, 1088–1096. [[CrossRef](#)]
32. Wang, S.; Shi, L.; Boubeche, M.; Wang, X.P.; Zeng, L.Y.; Wang, H.Q.; Xie, Z.A.; Tan, W.; Luo, H.X. Influence of Ln elements (Ln = La, Pr, Nd, Sm) on the structure and oxygen permeability of Ca-containing dual-phase membranes. *Sep. Purif. Technol.* **2020**, *251*, 117361. [[CrossRef](#)]
33. Shi, L.; Wang, S.; Lu, T.N.; He, H.; Yan, D.; Lan, Q.; Xie, Z.A.; Wang, H.Q.; Boubeche, M.; Luo, H.X. Effects of Al content on the oxygen permeability through dual-phase membrane $60\text{Ce}_{0.9}\text{Pr}_{0.1}\text{O}_{2-\delta}$ - $40\text{Pr}_{0.6}\text{Sr}_{0.4}\text{Fe}_{1-x}\text{Al}_x\text{O}_{3-\delta}$. *Ceram. Int.* **2019**, *45*, 20033–20039. [[CrossRef](#)]
34. Luo, H.X.; Jiang, H.Q.; Klande, T.; Cao, Z.W.; Liang, F.Y.; Wang, H.H.; Caro, J. Novel cobalt-free, noble metal-free oxygen-permeable $40\text{Pr}_{0.6}\text{Sr}_{0.4}\text{FeO}_{3-\delta}$ - $60\text{Ce}_{0.9}\text{Pr}_{0.1}\text{O}_{2-\delta}$ dual-phase membrane. *Chem. Mater.* **2012**, *24*, 2148–2154. [[CrossRef](#)]
35. Dutta, P.; Pal, S.; Seehra, M.S.; Shi, Y.; Eyring, E.M.; Ernst, R.D. Concentration of Ce^{3+} and oxygen vacancies in cerium oxide nanoparticles. *Chem. Mater.* **2006**, *18*, 5144–5146. [[CrossRef](#)]
36. Aarathi, U.; Shukla, D.; Rengaraj, S.; Babu, K.S. Ordered to defect fluorite structural transition in $\text{Ce}_{1-x}\text{Nd}_x\text{O}_{2-\delta}$ system and its influence on ionic conductivity. *J. Alloys Compd.* **2020**, *838*, 155534. [[CrossRef](#)]
37. Sameshima, S.; Hirata, Y.; Ehira, Y. Structural change in Sm- and Nd-doped ceria under a low oxygen partial pressure. *J. Alloys Compd.* **2006**, *408–412*, 628–631. [[CrossRef](#)]
38. Chueh, W.C.; McDaniel, A.H.; Grass, M.E.; Hao, Y.; Jabeen, N.; Liu, Z.; Haile, S.M.; McCarty, K.F.; Hendrik Bluhm, H.; Gabaly, F.E. Highly enhanced concentration and stability of reactive Ce^{3+} on doped C_eO_2 surface revealed in operando. *Chem. Mater.* **2012**, *24*, 1876–1882. [[CrossRef](#)]
39. Zhu, X.F.; Liu, Y.; Cong, Y.; Yang, W.S. $\text{Ce}_{0.85}\text{Sm}_{0.15}\text{O}_{1.925}$ - $\text{Sm}_{0.6}\text{Sr}_{0.4}\text{Al}_{0.3}\text{Fe}_{0.7}\text{O}_3$ dual-phase membranes: One-pot synthesis and stability in a CO_2 atmosphere. *Solid State Ionics* **2013**, *253*, 57–63. [[CrossRef](#)]
40. Balaguer, M.; García-Fayos, J.; Solís, C.; Serra, J.M. Fast oxygen separation through SO_2 - and CO_2 -stable dual-phase membrane based on NiFe_2O_4 - $\text{Ce}_{0.8}\text{Tb}_{0.2}\text{O}_{2-\delta}$. *Chem. Mater.* **2013**, *25*, 4986–4993. [[CrossRef](#)]
41. García-Fayos, J.; Ruhl, R.; Navarrete, L.; Bouwmeester, H.J.M.; Serra, J.M. Enhancing oxygen permeation through Fe_2NiO_4 - $\text{Ce}_{0.8}\text{Tb}_{0.2}\text{O}_{2-\delta}$ composite membranes using porous layers activated with Pr_6O_{11} nanoparticles. *J. Mater. Chem. A* **2018**, *6*, 1201–1209. [[CrossRef](#)]
42. Cheng, S.Y.; Huang, H.; Ovtar, S.; Simonsen, S.B.; Chen, M.; Zhang, W.; Søgaard, M.; Kaiser, A.; Hendriksen, P.V.; Chen, C.S. High-performance microchanneled asymmetric $\text{Gd}_{0.1}\text{Ce}_{0.9}\text{O}_{1.95-\delta}$ - $\text{La}_{0.6}\text{Sr}_{0.4}\text{FeO}_{3-\delta}$ -based membranes for oxygen separation. *ACS Appl. Mater. Interfaces* **2016**, *8*, 4548–4560. [[CrossRef](#)]
43. Balaguer, M.; Solís, C.; Serra, J.M. Structural-transport properties relationships on $\text{Ce}_{1-x}\text{Ln}_x\text{O}_{2-\delta}$ system (Ln = Gd, La, Tb, Pr, Eu, Er, Yb, Nd) and effect of cobalt addition. *J. Phys. Chem. C* **2012**, *116*, 7975–7982. [[CrossRef](#)]
44. Fang, W.; Liang, F.Y.; Cao, Z.W.; Steinbach, F.; Feldhoff, A. A Mixed ionic and electronic conducting dual-phase membrane with high oxygen permeability. *Angew. Chem. Int. Ed.* **2015**, *54*, 1–5. [[CrossRef](#)] [[PubMed](#)]
45. Nasani, N.; Shakel, Z.; Loureiro, F.J.A.; Panigrahi, B.B.; Kale, B.B.; Fagg, D.P. Exploring the impact of sintering additives on the densification and conductivity of $\text{BaCe}_{0.3}\text{Zr}_{0.55}\text{Y}_{0.15}\text{O}_{3-\delta}$ electrolyte for protonic ceramic fuel cells. *J. Alloys Compd.* **2021**, *862*, 158640. [[CrossRef](#)]

46. Taub, S.; Williams, R.E.A.; Wang, X.; McComb, D.W.; Kilner, J.A.; Atkinson, A. The effects of transition metal oxide doping on the sintering of cerium gadolinium oxide. *Acta Mater.* **2014**, *81*, 128–140. [[CrossRef](#)]
47. Shi, L.; Wang, S.; Lu, T.N.; He, Y.; Yan, D.; Lan, Q.; Xie, Z.A.; Wang, H.Q.; Li, M.R.; Caro, J.; et al. High CO₂-tolerance oxygen permeation dual-phase membranes Ce_{0.9}Pr_{0.1}O_{2-δ}-Pr_{0.6}Sr_{0.4}Fe_{0.8}Al_{0.2}O_{3-δ}. *J. Alloys Compd.* **2019**, *806*, 500–509. [[CrossRef](#)]
48. He, Y.; Shi, L.; Wu, F.; Xie, W.W.; Wang, S.; Yan, D.; Liu, P.J.; Li, M.R.; Caro, J.; Luo, H.X. A novel dual phase membrane 40wt% Nd_{0.6}Sr_{0.4}CoO_{3-δ}-60wt%Ce_{0.9}Nd_{0.1}O_{2-δ}: Design, synthesis and properties. *J. Mater. Chem. A* **2018**, *6*, 84–92. [[CrossRef](#)]
49. Steele, B.C.H. Oxygen ion conductors and their technological applications. *Mater. Sci. Eng. B* **1992**, *13*, 79. [[CrossRef](#)]
50. Kharton, V.V.; Tikhonovich, V.N.; Shuangbao, L.; Naumovich, E.N.; Yaremchenko, A.A. Ceramic microstructure and oxygen permeability of SrCo(Fe, M)O_{3-δ} (M = Cu or Cr) perovskite membranes. *J. Electrochem. Soc.* **1998**, *145*, 1363–1373. [[CrossRef](#)]
51. Shaula, A.L.; Fuentes, R.O.; Figueiredo, F.M.; Kharton, V.V.; Frade, J.R. Grain size effects on oxygen permeation in submicrometric CaTi_{0.8}Fe_{0.2}O_{3-δ} ceramics obtained by mechanical activation. *J. Euro. Ceram. Soc.* **2005**, *25*, 2613–2616. [[CrossRef](#)]
52. Sunarso, J.; Baumann, S.; Serra, J.M.; Meulenberg, W.A.; Liu, S.; Lin, S.Y.S.; Diniz da Costa, J.C. Mixed ionic-electronic conducting (MIEC) ceramic-based membranes for oxygen separation. *J. Membr. Sci.* **2008**, *320*, 13–41. [[CrossRef](#)]
53. Zeng, P.; Ran, R.; Chen, Z.; Gu, H.; Liu, S. Novel mixed conducting SrSc_{0.05}Co_{0.95}Co_{0.95}O_{3-δ} ceramic membrane for oxygen separation. *AIChE J.* **2010**, *53*, 3116–3124. [[CrossRef](#)]
54. Li, C.; Li, W.; Chew, J.; Liu, S.; Zhu, X.; Sunarso, J. Rate determining step in SDC-SSAF dual-phase oxygen permeation membrane. *J. Membr. Sci.* **2019**, *573*, 628–638. [[CrossRef](#)]
55. Zhang, C.; Sunarso, J.; Liu, S. Designing CO₂-resistant oxygen-selective mixed ionic-electronic conducting membranes: Guidelines, recent advances, and forward directions. *Chem. Soc. Rev.* **2017**, *46*, 2941–3005. [[CrossRef](#)] [[PubMed](#)]
56. Liang, F.; Luo, H.; Partovi, K.; Ravkina, O.; Cao, Z.; Liu, Y.; Caro, J. A novel CO₂-stable dual phase membrane with high oxygen permeability. *Chem. Commun.* **2014**, *19*, 2451–2454. [[CrossRef](#)] [[PubMed](#)]
57. Partovi, K.; Bittner, M.; Caro, J. Novel CO₂-tolerant Al-containing membranes for high-temperature oxygen separation. *J. Mater. Chem. A* **2015**, *3*, 24008–24015. [[CrossRef](#)]
58. Arnold, M.; Wang, H.H.; Feldhoff, A. Influence of CO₂ on the oxygen permeation performance and the microstructure of perovskite-type (Ba_{0.5}Sr_{0.5})(Co_{0.8}Fe_{0.2})O_{3-δ} membranes. *J. Membr. Sci.* **2007**, *293*, 44–52. [[CrossRef](#)]
59. Wang, S.; Shi, L.; Boubeche, M.; Wang, H.Q.; Xie, Z.A.; Tan, W.; He, Y.; Yan, D.; Luo, H.X. The effect of Fe/Co ratio on the structure and oxygen permeability of Ca-containing composite membranes. *Inorg. Chem. Front.* **2019**, *6*, 2885–2893. [[CrossRef](#)]
60. Wang, S.; Shi, L.; Xie, Z.A.; He, Y.; Yan, D.; Li, M.R.; Caro, J.; Luo, H.X. High-flux dual-phase percolation membrane for oxygen separation. *J. Eur. Ceram. Soc.* **2019**, *39*, 4882–4890. [[CrossRef](#)]